



Mathematical models of a biosensor

N.D. Botkin *, V.L. Turova

Center of Advanced European Studies and Research, Ludwig-Erhard-Allee 2, 53175 Bonn, Germany

Received 2 January 2003; received in revised form 2 October 2003; accepted 27 October 2003

Abstract

This paper studies mathematical models of a biosensor that serves for the measurement of small amounts of certain substances in liquids. The device works as follows: acoustic shear waves are excited due to an alternate voltage applied to electrodes deposited on a quartz crystal substrate; the waves are transmitted into a thin isotropic guiding layer in contact with a liquid containing molecules to be detected; these molecules adhere to a specific receptor, aptamer, immobilized on the surface of the guiding layer; the arising mass loading causes a phase shift in the electric signal which is measured on output electrodes. We state a three-dimensional mathematical model that describes a composite structure consisting of three coupled layers: two solid layers with different elastic and electric properties and a liquid layer treated as a weakly compressible viscous fluid. The full coupling between deformations and the electric field is assumed. A two-dimensional model is derived from the three-dimensional one by neglecting the non-homogeneity in x_2 -direction. Another two-dimensional model is derived by the averaging of the three-dimensional model in x_3 -direction under the assumption of an exponential attenuation of waves in the liquid and the substrate. The models are implemented numerically with finite elements. Computer simulations exhibit a good agreement with physical experiments.

© 2003 Elsevier Inc. All rights reserved.

Keywords: Love waves; Multi-layered structure; Fluid–solid interface; Finite element models

1. Introduction

One very promising applications of acoustic wave sensors is the measurement of small amounts of chemical and biological substances which possibly exist in liquids (see e.g., [1–3]). A biosensor, or microbalance, that serves for the quantitative detection of proteins is under development at the

* Corresponding author.

E-mail addresses: botkin@caesar.de (N.D. Botkin), turova@caesar.de (V.L. Turova).

Center of Advanced European Studies and Research (caesar) in Bonn. The binding of proteins is achieved due to the usage of highly selective nucleic acids called aptamers. An aptamer is located on the top of the guiding layer and contacts the liquid to be analysed. A wide variety of molecules including proteins, peptides or low molecular weight ligands can be targeted by aptamers. The application area of such biosensors includes clinical diagnosis, pharmaceutical analysis, food production and control. Since the deposited mass corresponds to the amount of bound molecules, the sensor can be used for real-time bioprocess monitoring.

A high sensitivity regarding to the mass loading is expected to be achieved due to the usage of shear horizontally polarized guided waves (Love waves) because of their low interaction with the contacting fluid. Fig. 1 presents a schematic picture of a Love wave sensor. A thin film, isotropic guiding layer, is deposited on a substrate made of a cut of a quartz crystal. The input and output interdigital transducers (IDTs) are located between the substrate and the guiding layer. To obtain purely shear polarized modes for which the displacements are parallel to x_2 -axis, the direction of the wave propagation is chosen to be orthogonal to crystallographic X -axis. The choice of the materials of the substrate and the guiding layer must ensure the wave velocity in the guiding film being less than the one in the substrate so that the waves will be transferred into the guiding layer.

Traditional simplifications used in the mathematical modelling of such devices (see e.g., [4–6]) are related to the assumption of the infiniteness in x_2 -direction, a simplified treatment of the fluid/solid interface, and the neglect of the mechanical influence of IDT fingers. These simplifications can be completely or partially dropped by using a rigorous mathematical model based on finite element (FE) method. The presented paper describes a three-dimensional FE-model that accounts:

- (1) finite dimensions of the sensor in all directions,
- (2) exact modelling of the liquid and the fluid/solid interaction,
- (3) careful description of the IDTs taking into account their size, mass and electro-conductivity.

The technique developed in [7] is used for the derivation of the model. An a posteriori estimate of the computational accuracy is proposed when the model is approximated by finite elements. Two reduced 2D-models of the biosensor are derived from the base 3D-model. The models are numerically implemented with the FE-program FeliCs [8] developed at the Technical University of Munich. The sparse linear algebra in FeliCs is supported by a parallelized version of the program SPOOLES (see [9]). A MAPLE code for the automatic derivation of model equations is

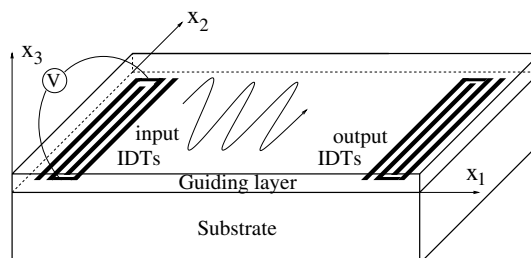


Fig. 1. Schematic picture of the sensor.

developed. This code computes the total energy and its variations in a symbolic form. This yields the model equations in a form appropriate for the input of FeliCs.

Numerical simulations related to a real biosensor are done. The results are being compared with physical experiments performed at the research center caesar.

2. Statement of a 3D-model

We consider linear material laws for solids (see [10]) and neglect non-linear terms in the description of the fluid. This seems to be reasonable because the displacements and velocities are very small for the structure under consideration.

2.1. Equations for the fluid, substrate and guiding layer

Let $u_1, u_2,$ and u_3 be the displacements in $x_1, x_2,$ and x_3 -directions, respectively; φ the electric potential; $v_1, v_2,$ and v_3 the velocity components; p the pressure; $\varrho, \rho^{(g)},$ and $\rho^{(s)}$ the densities of the fluid, the guiding layer, and the substrate, respectively. Open regions occupied by the fluid, the guiding layer, and the substrate are denoted by Ω with the subscripts $f, g,$ and $s,$ respectively. The notation $w_{x_i}, w_{x_i x_j}, w_t,$ and w_{tt} means the partial derivatives $\frac{\partial w}{\partial x_i}, \frac{\partial^2 w}{\partial x_i \partial x_j}, \frac{\partial w}{\partial t},$ and $\frac{\partial^2 w}{\partial t^2},$ respectively. Bold letters indicate vectors i.e., $\mathbf{u} = (u_1, u_2, u_3), \mathbf{v} = (v_1, v_2, v_3).$ The summation over repeated indices is assumed.

In the fluid layer, the Stokes and mass conservation equations hold:

$$\varrho v_t - \nu \Delta \mathbf{v} - \left(\xi + \frac{1}{3} \nu \right) \nabla \operatorname{div} \mathbf{v} + \nabla p = 0, \quad x \in \Omega_f, \tag{1}$$

$$\varrho_t + \operatorname{div}(\varrho \mathbf{v}) = 0, \quad x \in \Omega_f. \tag{2}$$

Here, ν and ξ are the dynamic and bulk viscosities of the fluid, respectively. The term $(\xi + \frac{1}{3} \nu) \nabla \operatorname{div} \mathbf{v}$ will be neglected because $\nu, \xi,$ and $\operatorname{div} \mathbf{v}$ are small for weakly compressible fluids. The substitutive equation for weakly compressible fluids reads (see [11]):

$$\varrho = \varrho_0 + \left. \frac{\partial \varrho}{\partial p} \right|_{\varepsilon} (p - p_0).$$

Here, $\left. \frac{\partial \varrho}{\partial p} \right|_{\varepsilon}$ means the density change under a constant entropy. Letting $p_0 = 0,$ we obtain the following linearized mass conservation law:

$$\gamma p_t + \operatorname{div} \mathbf{v} = 0, \quad x \in \Omega_f, \tag{3}$$

where $\gamma = \frac{1}{\varrho_0} \left. \frac{\partial \varrho}{\partial p} \right|_{\varepsilon}$ is the compressibility of the fluid. In (1), the variable density ϱ is replaced by ϱ_0 because the second order terms are neglected.

The isotropic guiding layer is governed by the following linear elasticity equations:

$$\rho^{(g)} u_{itt} - \sigma_{x_j}^{(g)ij}(\mathbf{u}) - \operatorname{div}(\beta(x) \nabla u_{it}) = 0, \quad x \in \Omega_g. \tag{4}$$

Here, $\sigma^{(g)ij}(\mathbf{u}) = C^{(g)ijkl} \varepsilon_{kl}(\mathbf{u})$ is the stress tensor, $C^{(g)ijkl}$ is the elastic stiffness tensor, and $\varepsilon_{kl}(\mathbf{u}) = \frac{1}{2} (u_{kx_l} + u_{lx_k})$ is the strain tensor. The last term of (4) expresses a damping arising on the

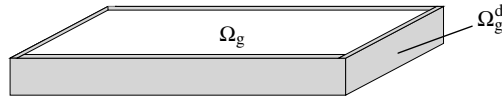


Fig. 2. Damping area of the guiding layer.

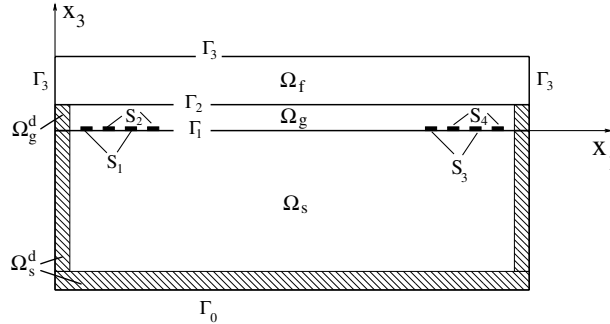


Fig. 3. Cross-section of the sensor by the plane $x_2 = 0$.

side boundaries of the device; $\beta(x)$ is a piecewise-linear function which is equal to zero outside of $\Omega_g^d \cup \Omega_s^d$ and grows up to some $\beta_0 > 0$ towards the side boundaries of the sensor. Fig. 2 shows the region Ω_g^d . The region Ω_s^d is sketched in Fig. 3 representing a cross-section of the sensor. Note that Ω_s^d includes a bottom layer of the substrate in addition to the side walls. In practice, some adhesive material like silicon caoutchouc is attached to the free faces of the device to avoid reflections on the boundaries. The conventional material for the guiding layer is silicon dioxide. Since this material does not possess piezoelectric properties, the influence of electric fields on the mechanical stress is negligible. We neglect the energy of the electric field in the guiding layer. Thus, the electric potential is not involved in Eq. (4).

For the piezoelectric substrate, the following electro-elasticity equations hold:

$$\rho^{(s)} u_{iit} - \sigma_{x_j}^{(s)ij}(\mathbf{u}, \varphi) + e^{kij} \varphi_{x_j x_k} - \text{div}(\beta(x) \nabla u_{it}) = 0, \quad x \in \Omega_s, \tag{5}$$

$$\epsilon^{ij} \varphi_{x_i x_j} + e^{kij} u_{ixk x_j} = 0, \quad x \in \Omega_s. \tag{6}$$

Here, $\sigma^{(s)ij}(\mathbf{u}, \varphi) = C^{(s)ijkl} \epsilon_{kl}(\mathbf{u}) - e^{kij} \varphi_{x_k}$ is the stress tensor, $C^{(s)ijkl}$ is the elastic stiffness tensor, ϵ^{ij} and e^{kij} are the material dielectric and piezoelectric stress tensors, $\varphi_{x_k} = E_k$ are components of the electric field. We will use the notation $\tilde{\sigma}^{(s)ij}(\mathbf{u}) = C^{(s)ijkl} \epsilon_{kl}(\mathbf{u})$. Indices i, j, k, l assume values 1, 2, 3.

The electrodes made of gold are homogeneous and isotropic. They are accounted through linear elasticity equations of the form:

$$\rho^{(e)} u_{iit} - \sigma_{x_j}^{(e)ij}(\mathbf{u}) = 0, \quad x \in \Omega_e,$$

where Ω_e is the region occupied by the input and output electrodes, $\rho^{(e)}$ and $\sigma^{(e)ij}$ are the gold density and the stress tensor related to gold, respectively. For simplicity of the presentation, we will not involve the above equations into the forthcoming weak formulation of the general 3D-

model. In Section 6, we show how the weak formulation should be modified in the case of reduced models to account the electrodes.

2.2. Interface and boundary conditions

Fig. 3 represents the cross-section of the biosensor by the plane $x_2 = 0$. The regions occupied by the guiding layer, the substrate, and the fluid are labeled as Ω_g , Ω_s , and Ω_f , respectively. The interface between Ω_g and Ω_s is denoted by Γ_1 , the boundary between Ω_g and Ω_f is Γ_2 . The external boundaries of the solid and fluid parts are Γ_0 and Γ_3 , respectively. Two alternated groups of the input IDTs are indicated as S_1 and S_2 , the output IDTs as S_3 and S_4 . All of the electrodes of each group are connected electrically. The electrodes of the groups S_1 and S_4 are supposed to be grounded.

Let n_j be the components of the normal vector \mathbf{n} to a region. The following interface and boundary conditions are posed:

- (a) Absence of forces on Γ_0 : $\sigma^{(g)ij}(\mathbf{u})n_j = 0, \sigma^{(s)ij}(\mathbf{u})n_j = 0$.
- (b) Continuity of the displacement field on Γ_1 and on the boundaries of the input and output electrodes.
- (c) Equilibrium of the pressures on Γ_1 : $\sigma^{(g)ij}(\mathbf{u})n_j = \sigma^{(s)ij}(\mathbf{u})n_j$, and similar conditions on the boundaries of input and output electrodes.
- (d) Dirichlet conditions for the electric potential: $\varphi|_{S_1} = 0, \varphi|_{S_2} = V(t), \varphi|_{S_4} = 0$, and the conductivity condition for the output electrodes: $\varphi|_{S_3} = C(t)$. Here, $V(t)$ is a prescribed exciting voltage whereas $C(t)$ is the output voltage to be determined from the model.
- (e) Neumann condition for the electric potential: $\frac{\partial \varphi}{\partial \mathbf{n}} = 0$ for (x_1, x_2) outside IDTs.
- (f) Equilibrium of the pressures on Γ_2 : $v \frac{\partial v_i}{\partial \mathbf{n}} - p_i = \sigma^{(g)ij}(\mathbf{u})n_j$, where \mathbf{n} is the outer normal to the solid part.
- (g) Continuity of the velocity on Γ_2 : $\frac{\partial \mathbf{u}}{\partial t} = \mathbf{v}$.
- (h) No-slip condition on Γ_3 : $\mathbf{v} = \mathbf{0}$.

Condition (g) is the most difficult to fulfill because it is not embedded into the weak formulation of the model equations. The following method from [12] is used to treat the problem. A new variable \mathbf{w} is introduced and the variable transformation

$$\mathbf{u} = \mathbf{u}_0 + \int_0^t \mathbf{w} \, d\tau \tag{7}$$

in Eqs. (4)–(6) and boundary conditions (a), (c), (f), (g), and (h) is performed. Obviously, relation (g) transforms into the natural condition: $\mathbf{w} = \mathbf{v}$ on Γ_2 .

3. Weak formulation of the problem

Denote $\Omega_{gs} = \text{int}(\overline{\Omega_g \cup \Omega_s})$ and $\Omega_{fgs} = \text{int}(\overline{\Omega_f \cup \Omega_g \cup \Omega_s})$. The symbol int means the interior of a set, the overline stands for the closure.

Using Eqs. (1),(3)–(6) and the above interface and boundary conditions yields the following weak formulation of the problem:

$$\begin{aligned} & \varrho_0 \int_{\Omega_f} \mathbf{v}_t \boldsymbol{\xi} \, dx + \nu \int_{\Omega_f} \nabla \mathbf{v} \nabla \boldsymbol{\xi} \, dx - \int_{\Omega_f} p \operatorname{div} \boldsymbol{\xi} \, dx + \gamma \int_{\Omega_f} p_t \zeta \, dx - \int_{\Omega_f} \operatorname{div} \mathbf{v} \zeta \, dx + \rho^{(g)} \int_{\Omega_g} \mathbf{w}_t \boldsymbol{\kappa} \, dx \\ & + \int_{\Omega_g} \sigma^{(g)ij}(\mathbf{u}) \boldsymbol{\kappa}_{jx_i} \, dx + \int_{\Omega_g^d} \beta(x) \nabla \mathbf{w} \nabla \boldsymbol{\kappa} \, dx + \rho^{(s)} \int_{\Omega_s} \mathbf{w}_t \boldsymbol{\kappa} \, dx + \int_{\Omega_s} \sigma^{(s)ij}(\mathbf{u}, \varphi) \boldsymbol{\kappa}_{jx_i} \, dx \\ & + \int_{\Omega_s^d} \beta(x) \nabla \mathbf{w} \nabla \boldsymbol{\kappa} \, dx + \int_{\Omega_s} \epsilon^{ij} \varphi_{x_j} \psi_{x_i} \, dx + \int_{\Omega_s} \epsilon^{kij} u_{ix_j} \psi_{x_k} \, dx = \int_{\Omega_s} f \, dx. \end{aligned} \tag{8}$$

Here $\boldsymbol{\xi}_j \in H_*^1(\Omega_f)$, $\zeta \in L_2(\Omega_f)$, $\boldsymbol{\kappa}_j \in H^1(\Omega_{gs})$, $\psi \in H_*^1(\Omega_s)$ are test functions with traces satisfying the interface conditions i.e. $\boldsymbol{\xi}_j = \boldsymbol{\kappa}_j$ on Γ_2 . Moreover, $H_*^1(\Omega_s)$ and $H_*^1(\Omega_f)$ denote functions from $H^1(\Omega_s)$ resp. $H^1(\Omega_f)$ with zero traces on $\overline{\Omega_s} \cap (S_1 \cup S_2 \cup S_4)$ resp. on Γ_3 . It is assumed that $\mathbf{u}_0 = \mathbf{0}$ so that $\mathbf{u} = \int_0^t \mathbf{w} \, d\tau$. The function f in the right-hand side of (8) arises due to Dirichlet boundary conditions for the electric potential (see item (d) of Section 2.2).

The following regularity can be proved using the technique of [12]. If $\mathbf{u}_0 = \mathbf{0}$, then the coupled system (8) obtained after the variable transformation (7) has a unique weak solution: $v_i \in L_2(0, T; H^1(\Omega_f))$, $w_i \in L_2(0, T; H^1(\Omega_{gs}))$, $\varphi \in L_2(0, T; H^1(\Omega_s))$, $p \in L_2(0, T; L_2(\Omega_f))$. As a consequence, $u_i \in H^1(0, T; H^1(\Omega_{gs}))$ so that the condition $v_i|_{\Gamma_2} = u_{it}|_{\Gamma_2}$ makes sense and holds for almost all $t \in [0, T]$. Here T is an arbitrary time instant.

4. Steady-state solutions

Let ω be the operating frequency of the IDTs, i.e. $V(t) = V_0 \sin \omega t$. We assume the following form of the solution:

$$\begin{aligned} \mathbf{u}(\mathbf{x}, t) &= -\frac{\mathbf{u}^{(1)}(\mathbf{x})}{\omega} \cos \omega t + \frac{\mathbf{u}^{(2)}(\mathbf{x})}{\omega} \sin \omega t, \\ \mathbf{w}(\mathbf{x}, t) &= \mathbf{u}_t(\mathbf{x}, t) = \mathbf{u}^{(1)}(\mathbf{x}) \sin \omega t + \mathbf{u}^{(2)}(\mathbf{x}) \cos \omega t, \\ \mathbf{v}(\mathbf{x}, t) &= \mathbf{v}^{(1)}(\mathbf{x}) \sin \omega t + \mathbf{v}^{(2)}(\mathbf{x}) \cos \omega t, \\ p(\mathbf{x}, t) &= p^{(1)}(\mathbf{x}) \sin \omega t + p^{(2)}(\mathbf{x}) \cos \omega t, \\ \varphi(\mathbf{x}, t) &= \varphi^{(1)}(\mathbf{x}) \sin \omega t + \varphi^{(2)}(\mathbf{x}) \cos \omega t. \end{aligned}$$

The substitution of this ansatz into (8) doubles the number of variables and test functions. If we express $p^{(1)}$ and $p^{(2)}$ through other unknowns using Eq. (3), we arrive at the following system:

$$\begin{aligned}
 & -\omega \varrho_0 \int_{\Omega_f} \mathbf{v}^{(2)} \xi^{(1)} \, dx + \nu \int_{\Omega_f} \nabla \mathbf{v}^{(1)} \nabla \xi^{(1)} \, dx + \frac{1}{\gamma \omega} \int_{\Omega_f} \operatorname{div} \mathbf{v}^{(2)} \operatorname{div} \xi^{(1)} \, dx + \omega \varrho_0 \int_{\Omega_f} \mathbf{v}^{(1)} \xi^{(2)} \, dx \\
 & + \nu \int_{\Omega_f} \nabla \mathbf{v}^{(2)} \nabla \xi^{(2)} \, dx - \frac{1}{\gamma \omega} \int_{\Omega_f} \operatorname{div} \mathbf{v}^{(1)} \operatorname{div} \xi^{(2)} \, dx - \omega \rho^{(g)} \int_{\Omega_g} \mathbf{u}^{(2)} \boldsymbol{\kappa}^{(1)} \, dx \\
 & + \frac{1}{\omega} \int_{\Omega_g} \sigma^{(g)ij}(\mathbf{u}^{(2)}) \kappa_{jxi}^{(1)} \, dx + \int_{\Omega_g^d} \beta(x) \nabla \mathbf{u}^{(1)} \nabla \boldsymbol{\kappa}^{(1)} \, dx + \omega \rho^{(g)} \int_{\Omega_g} \mathbf{u}^{(1)} \boldsymbol{\kappa}^{(2)} \, dx - \frac{1}{\omega} \int_{\Omega_g} \sigma^{(g)ij}(\mathbf{u}^{(1)}) \kappa_{jxi}^{(2)} \, dx \\
 & + \int_{\Omega_g^d} \beta(x) \nabla \mathbf{u}^{(2)} \nabla \boldsymbol{\kappa}^{(2)} \, dx - \omega \rho^{(s)} \int_{\Omega_s} \mathbf{u}^{(2)} \boldsymbol{\kappa}^{(1)} \, dx + \frac{1}{\omega} \int_{\Omega_s} \tilde{\sigma}^{(s)ij}(\mathbf{u}^{(2)}) \kappa_{jxi}^{(1)} \, dx - \int_{\Omega_s} e^{kij} \varphi_{xk}^{(1)} \kappa_{jxi}^{(1)} \, dx \\
 & + \int_{\Omega_s^d} \beta(x) \nabla \mathbf{u}^{(1)} \nabla \boldsymbol{\kappa}^{(1)} \, dx + \omega \rho^{(s)} \int_{\Omega_s} \mathbf{u}^{(1)} \boldsymbol{\kappa}^{(2)} \, dx - \frac{1}{\omega} \int_{\Omega_s} \tilde{\sigma}^{(s)ij}(\mathbf{u}^{(1)}) \kappa_{jxi}^{(2)} \, dx - \int_{\Omega_s} e^{kij} \varphi_{xk}^{(2)} \kappa_{jxi}^{(2)} \, dx \\
 & + \int_{\Omega_s^d} \beta(x) \nabla \mathbf{u}^{(2)} \nabla \boldsymbol{\kappa}^{(2)} \, dx + \int_{\Omega_s} \epsilon^{ij} \varphi_{xj}^{(1)} \psi_{xi}^{(1)} \, dx + \frac{1}{\omega} \int_{\Omega_s} e^{kij} u_{ixj}^{(2)} \psi_{xk}^{(1)} \, dx \\
 & + \int_{\Omega_s} \epsilon^{ij} \varphi_{xj}^{(2)} \psi_{xi}^{(2)} \, dx - \frac{1}{\omega} \int_{\Omega_s} e^{kij} u_{ixj}^{(1)} \psi_{xk}^{(2)} \, dx = \int_{\Omega_s} f \psi^{(1)} \, dx. \tag{9}
 \end{aligned}$$

Time-independent functions $\mathbf{u}^{(i)}, \mathbf{v}^{(i)}, \varphi^{(i)}, i = 1, 2$, satisfying (9) are called steady-state solutions corresponding to the operation frequency ω . Let us rename $\mathbf{v}^{(i)}$ to $\mathbf{u}^{(i)}$ (resp. $\xi^{(i)}$ to $\boldsymbol{\kappa}^{(i)}$) in the domain Ω_f using the fact that $\mathbf{v}^{(i)} = \mathbf{u}^{(i)}$ (resp. $\xi^{(i)} = \boldsymbol{\kappa}^{(i)}$) on the interface Γ_2 between Ω_f and Ω_g . The system (9) assumes the form:

$$\begin{aligned}
 & -\omega \varrho_0 \int_{\Omega_f} \mathbf{u}^{(2)} \boldsymbol{\kappa}^{(1)} \, dx + \nu \int_{\Omega_f} \nabla \mathbf{u}^{(1)} \nabla \boldsymbol{\kappa}^{(1)} \, dx + \frac{1}{\gamma \omega} \int_{\Omega_f} \operatorname{div} \mathbf{u}^{(2)} \operatorname{div} \boldsymbol{\kappa}^{(1)} \, dx + \omega \varrho_0 \int_{\Omega_f} \mathbf{u}^{(1)} \boldsymbol{\kappa}^{(2)} \, dx \\
 & + \nu \int_{\Omega_f} \nabla \mathbf{u}^{(2)} \nabla \boldsymbol{\kappa}^{(2)} \, dx - \frac{1}{\gamma \omega} \int_{\Omega_f} \operatorname{div} \mathbf{u}^{(1)} \operatorname{div} \boldsymbol{\kappa}^{(2)} \, dx - \omega \rho^{(g)} \int_{\Omega_g} \mathbf{u}^{(2)} \boldsymbol{\kappa}^{(1)} \, dx + \frac{1}{\omega} \\
 & \times \int_{\Omega_g} \sigma^{(g)ij}(\mathbf{u}^{(2)}) \kappa_{jxi}^{(1)} \, dx + \int_{\Omega_g^d} \beta(x) \nabla \mathbf{u}^{(1)} \nabla \boldsymbol{\kappa}^{(1)} \, dx + \omega \rho^{(g)} \int_{\Omega_g} \mathbf{u}^{(1)} \boldsymbol{\kappa}^{(2)} \, dx - \frac{1}{\omega} \\
 & \times \int_{\Omega_g} \sigma^{(g)ij}(\mathbf{u}^{(1)}) \kappa_{jxi}^{(2)} \, dx + \int_{\Omega_g^d} \beta(x) \nabla \mathbf{u}^{(2)} \nabla \boldsymbol{\kappa}^{(2)} \, dx - \omega \rho^{(s)} \int_{\Omega_s} \mathbf{u}^{(2)} \boldsymbol{\kappa}^{(1)} \, dx + \frac{1}{\omega} \\
 & \times \int_{\Omega_s} \tilde{\sigma}^{(s)ij}(\mathbf{u}^{(2)}) \kappa_{jxi}^{(1)} \, dx - \int_{\Omega_s} e^{kij} \varphi_{xk}^{(1)} \kappa_{jxi}^{(1)} \, dx + \int_{\Omega_s^d} \beta(x) \nabla \mathbf{u}^{(1)} \nabla \boldsymbol{\kappa}^{(1)} \, dx + \omega \rho^{(s)} \\
 & \times \int_{\Omega_s} \mathbf{u}^{(1)} \boldsymbol{\kappa}^{(2)} \, dx - \frac{1}{\omega} \int_{\Omega_s} \tilde{\sigma}^{(s)ij}(\mathbf{u}^{(1)}) \kappa_{jxi}^{(2)} \, dx - \int_{\Omega_s} e^{kij} \varphi_{xk}^{(2)} \kappa_{jxi}^{(2)} \, dx + \int_{\Omega_s^d} \beta(x) \nabla \mathbf{u}^{(2)} \nabla \boldsymbol{\kappa}^{(2)} \, dx \\
 & + \int_{\Omega_s} \epsilon^{ij} \varphi_{xj}^{(1)} \psi_{xi}^{(1)} \, dx + \frac{1}{\omega} \int_{\Omega_s} e^{kij} u_{ixj}^{(2)} \psi_{xk}^{(1)} \, dx + \int_{\Omega_s} \epsilon^{ij} \varphi_{xj}^{(2)} \psi_{xi}^{(2)} \, dx - \frac{1}{\omega} \int_{\Omega_s} e^{kij} u_{ixj}^{(1)} \psi_{xk}^{(2)} \, dx \\
 & = \int_{\Omega_s} f \psi^{(1)} \, dx. \tag{10}
 \end{aligned}$$

Let

$$a(\mathbf{u}^{(1)}, \mathbf{u}^{(2)}, \varphi^{(1)}, \varphi^{(2)}; \boldsymbol{\kappa}^{(1)}, \boldsymbol{\kappa}^{(2)}, \psi^{(1)}, \psi^{(2)})$$

be the bilinear form representing the left side of the system (10). It is not difficult to prove that the form a satisfies the following conditions:

$$(i) \ a(\mathbf{u}^{(1)}, \mathbf{u}^{(2)}, \varphi^{(1)}, \varphi^{(2)}; \mathbf{u}^{(1)}, \mathbf{u}^{(2)}, \omega\varphi^{(2)}, -\omega\varphi^{(1)}) \geq \mu_1 \left(\|\mathbf{u}^{(1)}\|_{H^1(\Omega_f)}^2 + \|\mathbf{u}^{(2)}\|_{H^1(\Omega_f)}^2 \right),$$

$$(ii) \ a(\mathbf{u}^{(1)}, \mathbf{u}^{(2)}, \varphi^{(1)}, \varphi^{(2)}; \omega\mathbf{u}^{(2)}, -\omega\mathbf{u}^{(1)}, \omega^2\varphi^{(1)}, \omega^2\varphi^{(2)}) \geq \mu_2 \left(\|\mathbf{u}^{(1)}\|_{H^1(\Omega_{gs})/Z}^2 + \|\mathbf{u}^{(2)}\|_{H^1(\Omega_{gs})/Z}^2 + \omega^2\|\varphi^{(1)}\|_{H^1(\Omega_s)}^2 + \omega^2\|\varphi^{(2)}\|_{H^1(\Omega_s)}^2 \right) - \omega^2\varrho_0\|\mathbf{u}^{(1)}\|_{L_2(\Omega_f)}^2 - \omega^2\varrho_0\|\mathbf{u}^{(2)}\|_{L_2(\Omega_f)}^2 - \omega^2\rho^{(g)}\|\mathbf{u}^{(1)}\|_{L_2(\Omega_g)}^2 - \omega^2\rho^{(g)}\|\mathbf{u}^{(2)}\|_{L_2(\Omega_g)}^2 - \omega^2\rho^{(s)}\|\mathbf{u}^{(1)}\|_{L_2(\Omega_s)}^2 - \omega^2\rho^{(s)}\|\mathbf{u}^{(2)}\|_{L_2(\Omega_s)}^2.$$

Here μ_1 and μ_2 are positive constants, Z denotes the space of rigid motions of the domain Ω_{gs} , and $H^1(\Omega_{gs})/Z$ is the quotient space. Adding inequalities (i) and (ii) yields

$$\begin{aligned} & a(\mathbf{u}^{(1)}, \mathbf{u}^{(2)}, \varphi^{(1)}, \varphi^{(2)}; \omega\mathbf{u}^{(2)} + \mathbf{u}^{(1)}, \mathbf{u}^{(2)} - \omega\mathbf{u}^{(1)}, \omega\varphi^{(2)} + \omega^2\varphi^{(1)}, -\omega\varphi^{(1)} + \omega^2\varphi^{(2)}) \\ & \geq \mu \left(\|\mathbf{u}^{(1)}\|_{H^1(\Omega_{fgs})}^2 + \|\mathbf{u}^{(2)}\|_{H^1(\Omega_{fgs})}^2 + \omega^2\|\varphi^{(1)}\|_{H^1(\Omega_s)}^2 + \omega^2\|\varphi^{(2)}\|_{H^1(\Omega_s)}^2 \right) \\ & \quad - \omega^2\varrho_0\|\mathbf{u}^{(1)}\|_{L_2(\Omega_f)}^2 - \omega^2\varrho_0\|\mathbf{u}^{(2)}\|_{L_2(\Omega_f)}^2 - \omega^2\rho^{(g)}\|\mathbf{u}^{(1)}\|_{L_2(\Omega_g)}^2 - \omega^2\rho^{(g)}\|\mathbf{u}^{(2)}\|_{L_2(\Omega_g)}^2 \\ & \quad - \omega^2\rho^{(s)}\|\mathbf{u}^{(1)}\|_{L_2(\Omega_s)}^2 - \omega^2\rho^{(s)}\|\mathbf{u}^{(2)}\|_{L_2(\Omega_s)}^2, \end{aligned} \tag{11}$$

where $\mu = \min(\mu_1, \mu_2)$. We have used here that $\mathbf{u}^{(1)}$ and $\mathbf{u}^{(2)}$ are continuous on the interface Γ_2 between Ω_f and Ω_g . This allowed us to exclude the space Z of rigid motions.

Let

$$\begin{aligned} \tilde{a}(\mathbf{u}^{(1)}, \mathbf{u}^{(2)}, \varphi^{(1)}, \varphi^{(2)}; \boldsymbol{\kappa}^{(1)}, \boldsymbol{\kappa}^{(2)}, \psi^{(1)}, \psi^{(2)}) &= a(\mathbf{u}^{(1)}, \mathbf{u}^{(2)}, \varphi^{(1)}, \varphi^{(2)}; \boldsymbol{\kappa}^{(1)} + \omega\boldsymbol{\kappa}^{(2)}, \boldsymbol{\kappa}^{(2)} \\ & \quad - \omega\boldsymbol{\kappa}^{(1)}, \omega\psi^{(2)} + \omega^2\psi^{(1)}, -\omega\psi^{(1)} + \omega^2\psi^{(2)}). \end{aligned} \tag{12}$$

Then, Eq. (10) is equivalent to the following one:

$$\tilde{a}(\mathbf{u}^{(1)}, \mathbf{u}^{(2)}, \varphi^{(1)}, \varphi^{(2)}; \boldsymbol{\kappa}^{(1)}, \boldsymbol{\kappa}^{(2)}, \psi^{(1)}, \psi^{(2)}) = \omega^2(f, \psi^{(1)})_{L_2(\Omega_s)} + \omega(f, \psi^{(2)})_{L_2(\Omega_s)}. \tag{13}$$

Denote

$$\mathcal{U} = (\mathbf{u}^{(1)}, \mathbf{u}^{(2)}, \varphi^{(1)}, \varphi^{(2)}), \quad \mathcal{V} = (\boldsymbol{\kappa}^{(1)}, \boldsymbol{\kappa}^{(2)}, \psi^{(1)}, \psi^{(2)}),$$

$$H = L_2(\Omega_{fgs}) \times L_2(\Omega_{fgs}) \times L_2(\Omega_s) \times L_2(\Omega_s),$$

$$V = H_*^1(\Omega_{fgs}) \times H_*^1(\Omega_{fgs}) \times H_*^1(\Omega_s) \times H_*^1(\Omega_s),$$

$$W = H^2(\Omega_{fgs}) \times H^2(\Omega_{fgs}) \times H^2(\Omega_s) \times H^2(\Omega_s).$$

Here $H_*^1(\Omega_{fgs})$ contains functions from $H^1(\Omega_{fgs})$ with zero traces on Γ_3 .

Let $\tilde{V}^h \subset V$ be a finite element approximation of V with linear finite elements, h the diameter of elements.

Estimate (11) and definition (12) show that the form \tilde{a} satisfies the Gårding inequality (see [13, Section 2.4.3])

$$\tilde{a}(\mathcal{U}, \mathcal{U}) + \mathcal{C}\|\mathcal{U}\|_H^2 \geq \alpha\|\mathcal{U}\|_V^2,$$

with $\alpha = \mu$ and $\mathcal{C} = \omega^2 \max(\varrho_0, \rho^{(g)}, \rho^{(s)})$. Assume that the problem $\{\tilde{a}(\mathcal{U}, \mathcal{V}) = 0, \mathcal{V} \in V\}$ has only the trivial solution, i.e. ω is not a generalized eigenvalue of the problem (9) with zero right

side. Then the exact and finite element solutions \mathcal{U} and \mathcal{U}^h of the problem (13) satisfy the estimate (see [13, Sections 4.1.3 and 4.5.2])

$$\|\mathcal{U}^h - \mathcal{U}\|_V \leq c \inf_{\chi \in V^h} \|\mathcal{U} - \chi\|_V \leq c_1 \|\mathcal{U}\|_W h$$

for sufficiently small h . Using the Aubin–Nitsche technique (see e.g., [14]) yields:

$$\|\mathcal{U}^h - \mathcal{U}\|_H \leq c_1 c_2 \|\mathcal{U}\|_W h^2.$$

5. A posteriori estimate of the computation accuracy

Let Q be any of 14 components $v_j^{(i)}, u_j^{(i)}, \varphi^{(i)}, i = 1, 2, j = 1, 2, 3$ of the solution, and Ω the corresponding domain where Q is defined. We have proved that

$$\|Q - Q^h\|_{L_2(\Omega)} \leq c_1 c_2 \|Q\|_{H^2(\Omega)} h^2. \tag{14}$$

Let λ_0 be the wavelength, $N = \frac{\lambda_0}{h}$ the number of finite elements per wavelength. For oscillatory solutions, the following estimate can be derived

$$\|Q\|_{H^2(\Omega)} \leq \frac{c_3}{\lambda_0^2}. \tag{15}$$

(see Section 4.6.4 of [13]). Using (14) and (15), we obtain

$$\|Q - Q^h\|_{L_2(\Omega)} \leq \frac{C}{N^2} \tag{16}$$

with $C = c_1 c_2 c_3$. This estimate is not useful because the constant c_1 is proportional (see [13, Section 4.5.2]) to $(\omega \sqrt{\text{density/stiffness}})^3$ and can be sufficiently large. Instead of that, an a posteriori estimate can be derived as follows. Replacing N by $2N$ in (16) yields

$$\|Q - Q^{h/2}\|_{L_2(\Omega)} \leq \frac{C}{4N^2}. \tag{17}$$

Assume that

$$\frac{\|Q - Q^{h/2}\|_{L_2(\Omega)}}{\|Q - Q^h\|_{L_2(\Omega)}} \leq q < 1,$$

for sufficiently small h , which is very realistic because q is expected to be near to 1/4 due to (16) and (17). Subtracting (17) from (16) yields

$$\begin{aligned} \|Q - Q^h\|_{L_2(\Omega)}^2 - \|Q - Q^{h/2}\|_{L_2(\Omega)}^2 &= (Q^{h/2} - Q^h, Q - Q^h + Q - Q^{h/2}) \\ &\leq \|Q^{h/2} - Q^h\|_{L_2(\Omega)} \|Q - Q^h\|_{L_2(\Omega)} + \|Q^{h/2} - Q^h\|_{L_2(\Omega)} \|Q - Q^{h/2}\|_{L_2(\Omega)}. \end{aligned}$$

Therefore,

$$\begin{aligned} \|Q - Q^h\|_{L_2(\Omega)}^2 - q^2 \|Q - Q^h\|_{L_2(\Omega)}^2 &\leq \|Q^h - Q^{h/2}\|_{L_2(\Omega)} \|Q - Q^h\|_{L_2(\Omega)} \\ &\quad + \|Q^h - Q^{h/2}\|_{L_2(\Omega)} q \|Q - Q^h\|_{L_2(\Omega)} \end{aligned}$$

for small h , which implies the estimate

$$\|Q - Q^h\|_{L_2(\Omega)} \leq \frac{1}{1-q} \|Q^h - Q^{h/2}\|_{L_2(\Omega)}. \tag{18}$$

A verification of this estimate will be done at the end of Section 6.2.

6. Reduced models: simulation results

Our goal is to simulate real devices whose operating frequency lies in the range of 80–130 MHz and the periodicity of the input and output IDTs is equal to 40 μm . Here and below, usual (not angular) frequencies are given. The thickness of the substrate is 0.5 mm, and the thickness of the guiding layer lies between 4 and 8 μm . The x_1 -length of the sensor is varied from 3 to 6.5 mm, x_2 -width is about 3 mm. The number of finite elements needed to simulate such a device, should be about 10^8 . It can hardly be achieved even on powerful workstations like SUN ULTRA60 being at our disposal. For this reason, the simulations were performed for reduced 2D-models described below in Sections 6.1 and 6.2.

Both of the reduced models take into account the mass of the electrodes by means of the terms

$$-\omega\rho^{(e)} \int_{\Omega_e} \mathbf{u}^{(2)} \boldsymbol{\kappa}^{(1)} dx + \frac{1}{\omega} \int_{\Omega_e} \sigma^{(e)ij}(\mathbf{u}^{(2)}) \kappa_{jxi}^{(1)} dx + \omega\rho^{(e)} \int_{\Omega_e} \mathbf{u}^{(1)} \boldsymbol{\kappa}^{(2)} dx - \frac{1}{\omega} \int_{\Omega_e} \sigma^{(e)ij}(\mathbf{u}^{(1)}) \kappa_{jxi}^{(2)} dx,$$

added to Eq. (9). Note that the x_3 -averaging of the electrodes can be easily done assuming that all functions in the above formula do not depend on x_3 . Such an averaging is reasonable because the thickness of the electrodes lies in the range from 200 to 300 nm.

The following material parameters are used in numerical simulations. The fluid is water with $\nu = 0.001 \text{ kg m}^{-1} \text{ s}^{-1}$. The guiding layer is made of SiO_2 with $\rho^{(g)} = 2180 \text{ kg m}^{-3}$, $\nu^{(g)} = 0.17$ and $E^{(g)} = 72 \text{ GPa}$; the electrodes are made of gold with $\rho^{(e)} = 19300 \text{ kg m}^{-3}$, $\nu^{(e)} = 0.44$ and $E^{(e)} = 78 \text{ GPa}$. The notations $\nu^{(\cdot)}$ and $E^{(\cdot)}$ mean, as usually, the Poisson ratio and the Young module of a material, respectively. For the substrate, CT- and ST-cuts of an α -quartz crystal (see [10]) are utilized. Fig. 4 explains the fabrication of some often used Y -rotated crystal cuts.

Numerical values of material constants for the non-rotated α -quartz possessing the trigonal crystal symmetry [10] are given in Table 1. The Voigt notation is used so that the following reduction of indices is applied $1 \leftrightarrow (11)$; $2 \leftrightarrow (22)$; $3 \leftrightarrow (33)$; $4 \leftrightarrow (23), (32)$; $5 \leftrightarrow (13), (31)$; $6 \leftrightarrow (12), (21)$. The usage of rotated crystal cuts demands a transformation of the elastic stiffness tensor, the

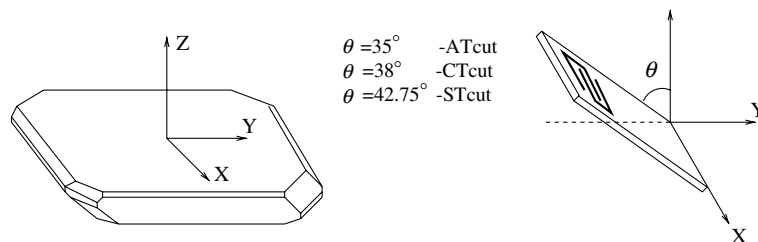


Fig. 4. Y -rotated cuts of α -quartz.

Table 1
Material constants for α -quartz

Density [kg m ⁻³]	$\rho^{(s)}$						
	2650						
Elastic stiffnesses [10 ⁹ N m ⁻²]	$C^{(s)11}$	$C^{(s)12}$	$C^{(s)13}$	$C^{(s)14}$	$C^{(s)33}$	$C^{(s)44}$	$C^{(s)66}$
	86.74	6.99	11.91	-17.91	107.2	57.94	39.88
Piezoelectric coefficients [C m ⁻²]	e^{11}	e^{14}	Dielectric coefficients		ϵ^{11}	ϵ^{33}	
	0.171	-0.0407	[10 ⁻¹² F m ⁻¹]		39.97	41.03	

dielectric tensor, and the piezoelectric stress tensor. Such a transformation is involved into the MAPLE code which derives model equations depending on the desired crystal cut.

6.1. An (x_1, x_3) -model

We assume that all variables in (9) do not depend on the coordinate x_2 . The integration over x_2 results in multiplication with the x_2 -length of the sensor. The integration over (x_1, x_3) is performed over the cross-sections of the regions Ω_f , Ω_g , and Ω_s by the plane $x_2 = 0$. The discretization is done using linear triangular finite elements being right-angled triangles whose legs are sufficiently small to resolve the actual wavelength (usually 40 μ m).

Fig. 5(a)–(c) show a steady-state solution in the fluid, guiding layer, and substrate, respectively. The vertical axis in Fig. 5(a) measures x_2 -velocity in the fluid (the function $v_2^{(1)}$ in (9)). In Fig. 5(b) and (c), the vertical axis measures x_2 -displacements (the function $u_2^{(2)}/\omega$). The computation is done for a short sensor (≈ 3 mm) equipped by three pairs of the input and output IDTs. The thickness of the electrodes is 0.25 μ m, the thicknesses of the guiding layer and the substrate are 7 μ m and 500 μ m, respectively. The periodicity λ of the input and output IDTs is 40 μ m, the operating frequency is equal to 81 MHz. A strong attenuation of waves in the substrate and a good wave transfer into the guiding layer is clearly visible, which is expected theoretically for Love waves. In accordance with the theory [11], the penetration depth of waves into the fluid lies in the range of one wave length.

Simulations of a long sensor (6.5 mm) with 50 pairs of the input and output electrodes is also performed. The so called insertion loss which expresses the ratio of the output and input signals is computed for such a sensor. Remember that the insertion loss is defined as

$$20 \lg \left(\sqrt{\left(\varphi_{|S_3}^{(1)}\right)^2 + \left(\varphi_{|S_3}^{(2)}\right)^2} / V_0 \right),$$

where S_3 is the area occupied by the non-grounded output electrodes, and V_0 is the amplitude of the exciting voltage. Fig. 6 presents the insertion loss versus the operating frequency. The highest sharp peak near 118 MHz corresponds to the resonance frequency.

A high sensitivity of the model with respect to small mass loadings is also proved. In Fig. 7, the dependence of the device sensitivity on the thickness of the guiding layer is shown. The sensitivity is being computed as the phase shift in the electric signal divided by the mass loading per a surface unit. The mass loading is modeled through an additional thin gold layer averaged in x_3 -direction.

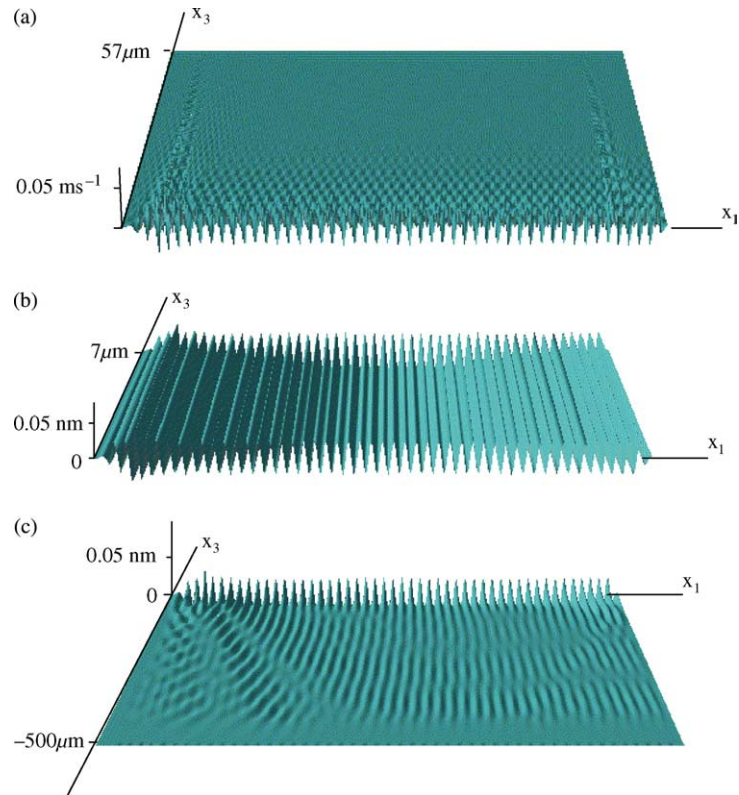


Fig. 5. Steady-state solution for (x_1, x_3) -model. (a) x_2 -component of the velocity field in the fluid; (b and c): x_2 -component of the displacement field in the guiding layer and substrate, respectively.

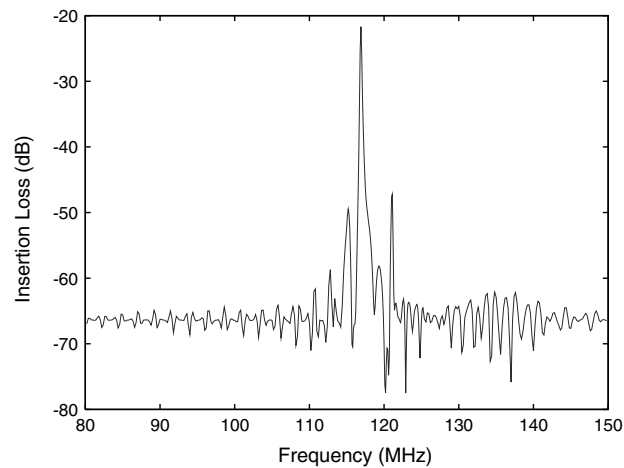


Fig. 6. Insertion loss versus the operating frequency for (x_1, x_3) -model.

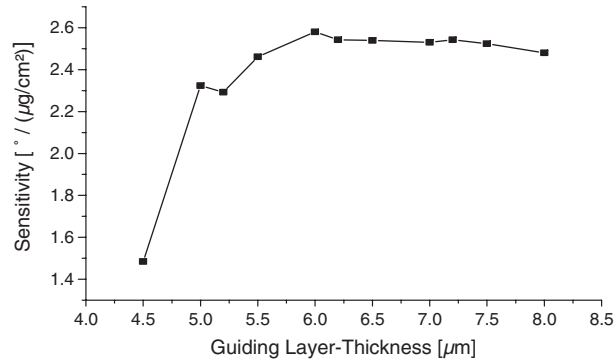


Fig. 7. Influence of the thickness of the guiding layer on the sensitivity.

The best sensitivity is attained at the thickness of 6 µm, which is in accordance with the literature (see e.g., [2]).

Fig. 8 shows the geometry of a test device built for the experimental study of various effects. The mass loading, a molecular film adhering to the substrate surface, is modeled by a gold layer of $d = 2$ mm length deposited between the input and output IDTs. Numerical simulations for such a device are in a good agreement with the value obtained from physical experiments. For example, the resonance frequency of 128 MHz obtained from the numerical simulation shown in Fig. 9 is very close to the experimental value.

6.2. An (x_1, x_2) -model

In the (x_1, x_3) -model described above, all values were assumed being independent on x_2 -coordinate. In the reality, the sensor and the electrodes are bounded in x_2 -direction, which may cause reflections on their boundaries. To study the influence of these effects on the propagation of Love waves, the following (x_1, x_2) -model is proposed.

Let h , δ , and r be the thicknesses of the substrate, the guiding layer, and the liquid layer, respectively. We assume that the displacement field, the electric potential, the velocity field in the fluid, and the pressure can be represented in the form

$$\mathbf{u}(x_1, x_2, x_3) = \psi(x_3)\mathbf{U}(x_1, x_2), \quad (x_1, x_2) \in \Omega_{sg}, \quad x_3 \in [-h, \delta],$$

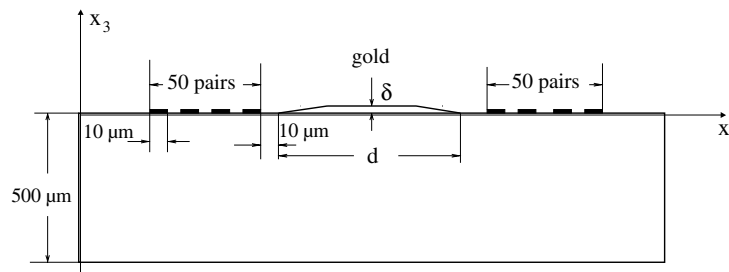


Fig. 8. Geometry of an experimental device.

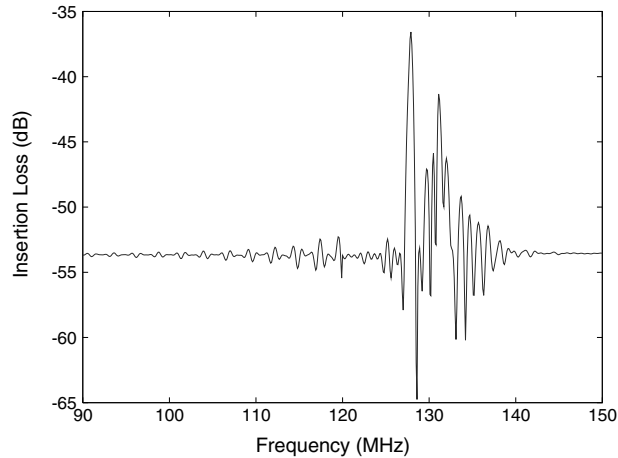


Fig. 9. Insertion loss versus the operating frequency for (x_1, x_3) -model of the experimental device.

$$\varphi(x_1, x_2, x_3) = \psi(x_3)\Phi(x_1, x_2), \quad (x_1, x_2) \in \Omega_s, \quad x_3 \in [-h, 0],$$

$$\mathbf{v}(x_1, x_2, x_3) = \psi(x_3)\mathbf{V}(x_1, x_2), \quad (x_1, x_2) \in \Omega_f, \quad x_3 \in [\delta, \delta + r],$$

$$p(x_1, x_2, x_3) = \psi(x_3)P(x_1, x_2), \quad (x_1, x_2) \in \Omega_f, \quad x_3 \in [\delta, \delta + r],$$

where \mathbf{U} , Φ , \mathbf{V} , and P are unknown functions, and the function ψ is defined as follows:

$$\psi(x_3) = \begin{cases} \left(1 - \exp\frac{a(x_3 + h)}{h}\right) / (1 - \exp a), & x_3 \in [-h, 0] \\ 1, & x_3 \in [0, \delta] \\ \left(1 - \exp\frac{b(\delta + r - x_3)}{r}\right) / (1 - \exp b), & x_3 \in [\delta, \delta + r], \end{cases}$$

so that the conditions

$$\psi(0) = 1, \quad \psi(-h) = 0, \quad \psi(\delta + r) = 0,$$

are satisfied (see Fig. 10). This assumption means that acoustic waves with some exponential attenuation in the substrate and in the liquid are exclusively considered. The values $a > 0$ and $b > 0$ specify the attenuation rate of waves. They can be obtained from simulations by means of the (x_1, x_3) -model. Since the sensor is cylindrical in x_3 , the integration over x_3 in (9) can be performed in an analytic form separately from the integration over (x_1, x_2) .

The simulation is done for another experimental sensor whose geometry is similar to that shown in Fig. 8 but the number of input and output IDT pairs is equal to 50. A triangulation similar to that used for (x_1, x_3) -model is utilized. The thickness δ of the gold layer is equal 0.2557 μm . The liquid layer is omitted for simplicity.

Fig. 11 shows the profile of horizontally polarized shear waves. The vertical axis measures x_2 -displacement (the function $u_2^{(2)}/\omega$). One can see that the reflections on the side boundaries of the sensor are eliminated. This is achieved due to an appropriate choice of the damping coefficient β_0 . The knowledge of β_0 is helpful when selecting suitable damping materials.

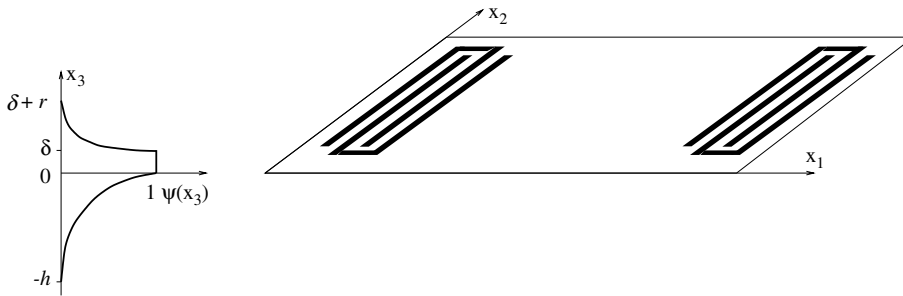


Fig. 10. (x_1, x_3) -model.

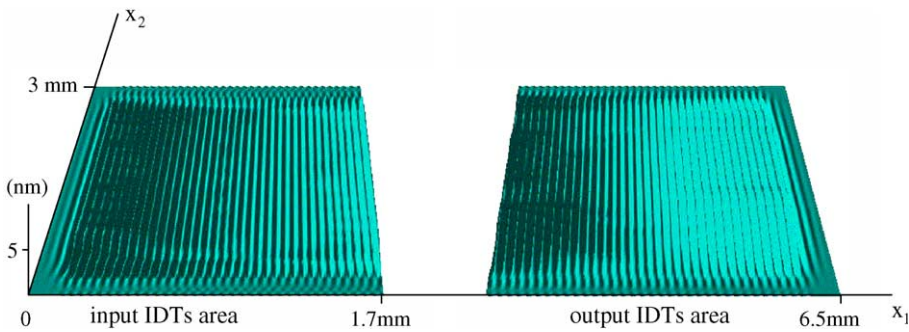


Fig. 11. Steady-state solution for (x_1, x_2) -model: the vertical axis measures x_2 -component of the displacement field on the substrate surface.

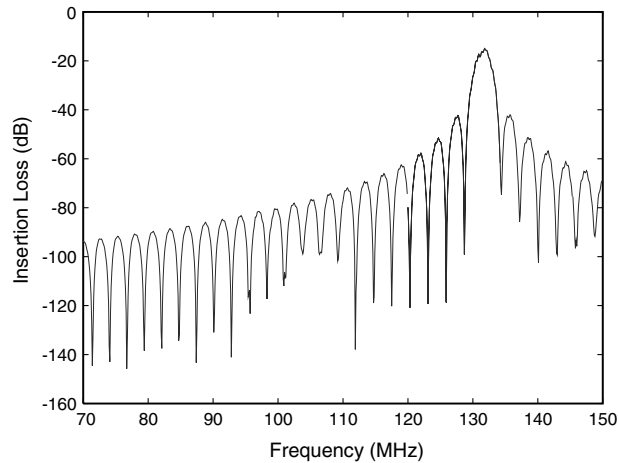


Fig. 12. Resonance peak for horizontally polarized shear waves in the case of an ST-cut of α -quartz. The electrodes are strictly parallel to the crystalline X -axis.

In addition to horizontally polarized shear waves, vertically polarized shear waves and longitudinal waves can be excited. In Fig. 12, a unique resonance peak at 132 MHz corresponds to

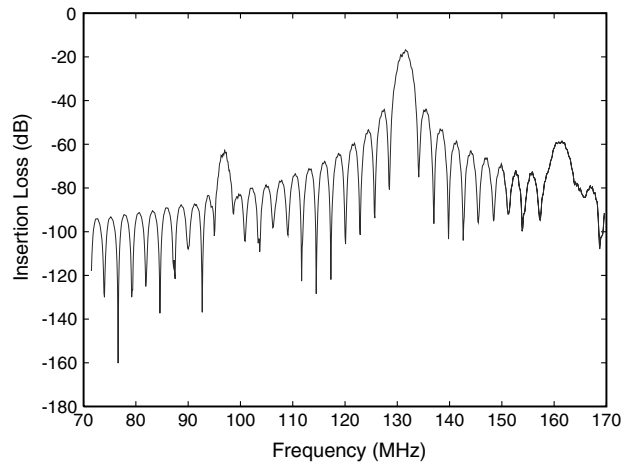


Fig. 13. Generation of vertically polarized shear waves and longitudinal waves due to the rotation of the electrodes through 3° . Formation of two additional resonance peaks related to these waves.

horizontally polarized shear waves. In Fig. 13, two additional resonance peaks at 98 and 160 MHz correspond to vertically polarized shear waves and longitudinal waves, respectively. The cause of the excitation of these modes is the rotation of the electrodes through 3° about x_3 -axis with respect to their nominal position.

Using (x_1, x_2) -model, a verification of the estimate (18) has been done. To this end, a sensor of $300 \mu\text{m} \times 300 \mu\text{m}$ surface size equipped by 3 pairs of the input and output electrodes is simulated. We did two computations using rectangular meshes 300×240 ($h \approx 1.6 \mu\text{m}$) and 150×120 and obtained $\|Q^h - Q^{h/2}\|_{L_2(\Omega)} = 0.046$. This yields the estimate of the order 0.06, if q in (18) is close to $1/4$.

7. Conclusions

A three-dimensional finite element model of a biosensor is developed. A heuristic estimate of the computational accuracy is proposed. The model can be either implemented directly on a powerful PC-cluster or used for the derivation of reduced two-dimensional models that speed up the simulation of real biosensing devices. Two such reduced models obtained through different averaging procedures are considered. Comparison of numerical and experimental results shows that reduced models are useful for the design of biosensing devices.

Acknowledgements

The authors are grateful to Professor K.-H. Hoffmann for his continuous attention to this work. We would like to thank Dr. M. Tewes and M. Schlensog from the research center caesar in Bonn for the experimental support of the work.

References

- [1] G. Kovacs, M.J. Vellekoop, R. Hauéis, et al., A Love wave sensor for (bio)chemical sensing in liquids, *Sens. Actuators A* 43 (1994) 38–43.
- [2] J. Du, G.L. Harding, J.A. Ogilvy, et al., A study of Love-wave acoustic sensors, *Sens. Actuators A* 56 (1996) 211–219.
- [3] B. Jakobi, M.J. Vellekoop, Viscosity sensing using a Love-wave device, *Sens. Actuators A* 68 (1998) 275–281.
- [4] H. Drobe, A. Leidl, M. Rost, et al., Acoustic sensors based on surface-localized HPSWs for measurements in liquids, *Sens. Actuators* 4 (1993) 141–148.
- [5] B. Jakobi, M.J. Vellekoop, Properties of Love waves: applications in sensors, *Smart Mater. Struct.* 6 (1997) 668–679.
- [6] J.A. Ogilvy, An approximate analysis of waves in layered piezoelectric plates from an interdigital source transducer, *J. Phys. D: Appl. Phys.* 29 (1996) 876–884.
- [7] K.-H. Hoffmann, N.D. Botkin, Oscillations of nonlinear thin plates excited by piezoelectric patches, *ZAMM* 78 (1998) 495–503.
- [8] I. Eichenseher, I.G. Götz, FeliCs—Intern Documentation, Manuscript, Chair of Applied Mathematics, Technical University of Munich, 1997.
- [9] C. Ashcraft, R. Grimes, SPOLES: an object-oriented sparse matrix library, in: B. Hendrickson et al. (Eds.), 9th SIAM Conference on Parallel Processing for Scientific Computing, San Antonio, Texas, March 1999.
- [10] J. Zelenka, Piezoelectric resonators and their applications, *Studies in Electrical and Electronic Engineering*, vol. 24, Elsevier, Amsterdam, 1986.
- [11] L.D. Landau, E.M. Lifschitz, *Hydrodynamik*, Akademie-Verlag, Berlin, 1975.
- [12] J.L. Lions, *Quelques Méthodes de Résolution des Problèmes aux Limites non Linéaires*, Dunod Gauthier-Villars, Paris, 1969.
- [13] F. Ihlenburg, *Finite Element Analysis of Acoustic Scattering*, Applied Mathematical Sciences, vol. 132, Springer-Verlag, New York, 1998.
- [14] P.G. Ciarlet, *The Finite Element Method for Elliptic Problems*, North-Holland, Amsterdam, 1978.